

Changing Molecular Gas Properties in the Bar and Center of NGC 7479

S. Hüttemeister¹, S. Aalto², M. Das^{3,4} W. F. Wall⁵

¹ Radioastronomisches Institut der Universität Bonn, Auf dem Hügel 71, D - 53121 Bonn, Germany

² Onsala Space Observatory, S - 43992 Onsala, Sweden

³ Indian Institute of Astrophysics, Bangalore, India

⁴ Department of Astronomy, University of Maryland, College Park, MD 20742, USA

⁵ INAOE, 72000 Puebla, Mexico

Received 19 March 2000 / Accepted 24 August 2000

Abstract. We present sensitive interferometric ^{12}CO , ^{13}CO and HCN observations of the barred spiral galaxy NGC 7479, known to be one of the few barred galaxies with a continuous gas-filled bar. We focus on the investigation and interpretation of $^{12}\text{CO}/^{13}\text{CO}$ line intensity ratios $\mathcal{R}_{12/13}$, which is facilitated by having more than 90% of the flux in our interferometer maps. The global (9 kpc by 2.5 kpc) value of $\mathcal{R}_{12/13}$ is high at 20 – 40. On smaller scales (~ 750 pc), $\mathcal{R}_{12/13}$ is found to vary dramatically, reaching values > 30 in large parts of the bar, but dropping to values ~ 5 , typical for galactic disks, at a ^{13}CO condensation in the southern part of the bar. We interpret these changes in terms of the relative importance of the contribution of a diffuse molecular component, characterized by unbound gas that has a moderate optical depth in the $^{12}\text{CO}(1\rightarrow 0)$ transition. This component dominates the ^{12}CO along the bar and is also likely to play an important role in the center of NGC 7479. In the center, the ^{12}CO and the HCN intensity peaks coincide, while the ^{13}CO peak is slightly offset. This can be explained in terms of high gas temperature at the ^{12}CO peak position. Along the bar, the relation between the distribution of ^{12}CO , ^{13}CO , dust lanes and velocity gradient is complex. A southern ^{13}CO condensation is found offset from the ^{12}CO ridge that generally coincides with the most prominent dust lanes. It is possible that strong ^{13}CO detections along the bar indicate quiescent conditions, downstream from the major bar shock. Still, these condensations are found close to high velocity gradients. In the central region, the velocity gradient is traced much more closely by ^{13}CO than by ^{12}CO .

Key words: galaxies: individual: NGC 7479 - galaxies: ISM - galaxies: starburst - radio lines: galaxies

1. Introduction

Bars are regarded as an important transport mechanism of material toward the central regions of galaxies, fuelling nuclear starbursts and driving galaxy evolution through the concentration of mass close to the nucleus (e.g. Sakamoto et al. 1999, Combes 1990 and references therein). To accomplish this, gas has to flow inward through the bar; however, long bars that are filled with dense gas that can be traced in CO are rare and thus likely transient. Among the few specimens known are NGC 1530 (Reynaud & Downes 1998), M 100 (Sempere & García-Burillo 1997), UGC 2855 (Hüttemeister et al. 1999), NGC 2903 and NGC 3627 (Regan et al. 1999). These bars differ significantly in their properties, i.e. velocity field, linewidth and derived shock structure. This is somewhat surprising, since the gas should in all cases be responding to a strong bar potential in a similar way. The dynamics of this response should then have consequences for the properties of the gas in the bar and the nucleus, e.g. produce a diffuse component unbound from clouds (e.g. Das & Jog 1995). The evolutionary state of the bar and the degree of central mass concentration may be instrumental in regulating the conditions of the gas in the bar (see models by Athanassoula 1992). More specifically, the gas is funnelled from outer x_1 -orbits to inner x_2 -orbits as the bar evolves in time (see e.g. the simulations by Friedli & Benz 1993).

To better understand the gas flow, the star formation efficiency along the bar and the feeding of a starburst, it is essential to know the physical state of the gas both along the bar and in the central structure. An analysis based on more molecules than ^{12}CO , the most abundant species after H_2 , is necessary to investigate gas properties and to go beyond the study of the morphological and kinematic structure of a system. Achieving this goal requires the detection and high-resolution mapping of very faint lines, observations which are at the sensitivity limit of today's millimeter interferometers.

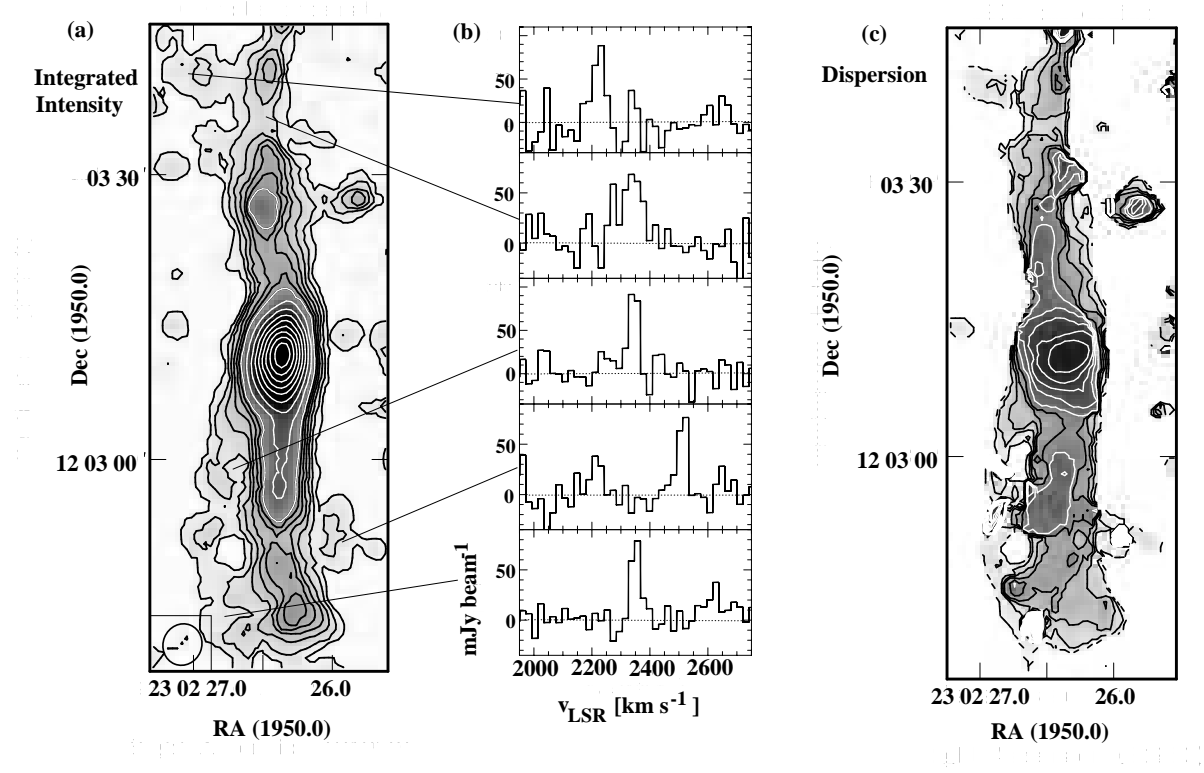


Fig. 1. (a) The map of the ^{12}CO (1 → 0) total integrated intensity. The contour levels range from 7.6 K km s^{-1} ($1.6 \text{ Jy beam}^{-1} \text{ km s}^{-1}$ or 1.5σ for a velocity width of 400 km s^{-1}) to 76 K km s^{-1} ($16 \text{ Jy beam}^{-1} \text{ km s}^{-1}$, 16σ) in steps of 11.4 K km s^{-1} ($2.4 \text{ Jy beam}^{-1} \text{ km s}^{-1}$, 2σ) (black), then change to a spacing of 38 K km s^{-1} ($8.0 \text{ Jy beam}^{-1} \text{ km s}^{-1}$, 8σ) up to 380 K km s^{-1} ($80 \text{ Jy beam}^{-1} \text{ km s}^{-1}$) (white). (b) Representative spectra from the outer regions of the maps, demonstrating that the lines in these regions become narrow, but are clearly detected. The spectra correspond to single beams centered on the positions indicated. (c) Dispersion map. The contours range from 10 km s^{-1} to 100 km s^{-1} in steps of 10 km s^{-1} . The peak dispersion is 110 km s^{-1} .

In this paper, we present such a study, carried out in one of the best known gas-rich barred galaxies, NGC 7479, classified a (mild) starburst SBb galaxy containing a LINER nucleus, has a gaseous bar of ~ 10 kpc projected length (for an assumed distance of $D = 32$ Mpc, see Table 1), which has been repeatedly mapped in ^{12}CO : Semper et al. (1995) present single dish data in the 1 → 0 and 2 → 1 transition. Interferometric 1 → 0 maps have been obtained by Quillen et al. (1995) and recently by Laine et al. (1999). Our results include the most sensitive ^{12}CO map to date, but we focus on the relation of the ^{12}CO emission to the first interferometric ^{13}CO (1 → 0) and HCN(1 → 0) data obtained in NGC 7479, and the physical state of the gas we can infer from the comparison of these molecules to the ^{12}CO distribution. Preliminary results of this study were given in Aalto et al. (1997a).

2. Observations

2.1. Interferometric observations at OVRO

We have obtained interferometric maps of the 1 → 0 transitions of ^{12}CO , ^{13}CO , HCN and in the inner 1' (9 kpc) of NGC 7479 using the Caltech six-element Owens Valley Radio Observatory (OVRO) millimeter array. All observations were centered on the radio continuum peak. The quasar 3C454.5 was observed every ~ 15 min as a phase and amplitude calibrator. 3C345 was used as an additional passband calibrator, and flux calibration was done relative to the planets Neptune and Uranus. Calibration was done with the standard package developed for OVRO. Continuum emission with a peak flux of $3 - 4 \text{ mJy beam}^{-1}$ has been subtracted from all maps.

The observations were carried out in the low resolution and equatorial configurations of the OVRO array between February and June 1996. The naturally weighted synthesized beam sizes are $4.^{\prime}6 \times 4.^{\prime}25$ for ^{12}CO , $4.^{\prime}9 \times 4.^{\prime}05$ for ^{13}CO and $7.^{\prime}2 \times 5.^{\prime}2$ for HCN. At $D=32$ Mpc, 1' equals 155 pc. The *positional accuracy* of structures in the maps is $\sim 0.^{\prime}5$ and thus considerably higher than the resolution. Due to the limited *uv*-coverage, the maps are not sensi-

Table 1. Adopted properties of NGC 7479

R.A. (1950.0) ^{a)}	Dec (1950.0) ^{a)}	Distance	Type ^{b)}	$m_b^b)$	$i^c)$	Size (blue) ^{b)}	$L_{\text{FIR}}^d)$	PA disk ^{e)}	PA bar ^{e)}
23 ^h 02 ^m 26.37 ^s	12° 03' 10.6"	32 Mpc	SBb	11 ^m 7 ^{c)}	~ 45°	4'.4 × 3'.4	$4 \cdot 10^{10} L_{\odot}$	25°	5°

a): Radio continuum peak position (Neff & Hutchings 1992, VLA A-Array at 1.490 MHz)

b): from the UGC catalogue (Nilson 1973)

c): from Groosbol (1985) i : angle of inclination

d): from Sempere et al. (1995)

e): Position angle (north-to-east) of the disk major axis (see e.g. the UGC catalogue) and the gaseous bar. The position angle of the stellar bar is even closer to that of the disk major axis (Sempere et al. 1995).

tive to structures larger than $\sim 15''$ for CO and $\sim 21''$ for HCN. On-source integration times were 7.2 hr for ^{12}CO , 23.5 hr for ^{13}CO and 11.5 hr for HCN.

The parameters of the observations are summarized in Table 2.

For a beamsize of $4''.4$, i.e. ^{12}CO , a brightness temperature (T_B) of 1 K corresponds to $0.210 \text{ Jy beam}^{-1}$ at a wavelength of 2.6 mm. The spectral resolution of our data is 4 MHz or 10.04 km s^{-1} , and the total velocity range covered by the autocorrelator is 1120 km s^{-1} , centered on $v_{\text{LSR}} = 2500 \text{ km s}^{-1}$. For the final presentation, the data were smoothed to a velocity resolution of 20 km s^{-1} (^{12}CO and ^{13}CO) or 40 km s^{-1} (HCN).

Imaging was done using the NRAO AIPS package. For image display and analysis of the data cubes, the ATNF Karma package was also used.

2.2. Single dish observations at OSO

Single dish spectra of the $1 \rightarrow 0$ transitions of ^{12}CO and ^{13}CO were taken at the Onsala Space Observatory 20 m telescope in 1997. The central position of NGC 7479 was observed with a beamsize of $33''$ and system temperatures of $500 \text{ K} - 600 \text{ K}$ (^{12}CO) and $200 \text{ K} - 300 \text{ K}$ (^{13}CO). The spectra were smoothed to a velocity resolution of 30 km s^{-1} .

3. Results

3.1. The Distribution of the ^{12}CO Emission

3.1.1. Morphology and Central Kinematics

The ^{12}CO distribution is displayed in Fig. 1a. It extends in one continuous structure over the whole length of the bar, with a number of secondary peaks along the bar axis. The total ^{12}CO flux in the map is 380 Jy km s^{-1} . The distribution has a central concentration with a (deconvolved) FWHM size of $7''.5 \times 2''.6$ ($1200 \times 400 \text{ pc}$ at $D=32 \text{ Mpc}$). This structure holds about 30 % of the total CO flux of the bar. The peak position is at $\alpha = 23^{\text{h}} 02^{\text{m}} 26.37^{\text{s}}$ and $\delta = 12^{\circ} 03' 11''.6$, coincident to within $1''.0$ with the radiocontinuum peak.

In Fig. 1b, we display some representative spectra from the outer parts of our ^{12}CO map, regions where the confi-

dence level of the integrated intensity maps (which refers to the full velocity width in the center of 400 km s^{-1}) drops below 2σ . The lines are clearly detected in these parts of the bar, but become very narrow. The same effect is evident from the dispersion map (Fig. 1c): The dispersion (calculated along the line-of-sight, δv_{mom}) falls off sharply toward the bar edges, but remains at 40 km s^{-1} to 60 km s^{-1} close to the major axis.

To show that the change in dispersion is not a result of projected rotation, we display position-velocity (pv) diagrams along the bar major axis (position angle (PA) 5° , Fig. 2a) and the disk major axis (PA 25° , Fig. 2c). The velocity width is not systematically larger along the disk major axis, where rotation should have the largest effect. Also, the regions of narrow lines are not associated with the disk minor axis. The only possible effect of rotation is a tentative alignment of the 60 km s^{-1} to 80 km s^{-1} velocity contours in the ^{12}CO dispersion map (Fig. 1c and Fig. 4a) with the disk major axis.

There is no sign of a ‘twin peaks’ structure (as coined by Kenney et al. 1992) perpendicular to the bar, perhaps suggesting that there are no x_2 antibar orbits, occurring within an Inner Lindblad resonance (ILR). However, the question of the existence of an ILR in NGC 7479 is controversial and remains undecided: Quillen et al. (1995) derived the existence of an ILR close to the nucleus, while in the models of Sempere et al. (1995) no ILR exists. Laine et al. (1998) argue that the bar perturbation close to the center is so strong that the issue cannot be resolved without non-linear orbit analysis. In any case, the ILR would be located within $700 \text{ pc} - 800 \text{ pc}$ ($4'' - 5''$) from the nucleus; thus, we would barely resolve a ‘twin peak’ structure.

Another possible signature of an ILR is a ring of material close to its positions, due to the expected pile-up of gas in the collision region where x_1 and x_2 orbits intersect. Such a structure may be indicated in our map. There certainly is a clear peak not just in intensity but also in velocity dispersion (Fig. 1c) in the center. This dispersion peak fragments into a high velocity system, consisting of a number of clumps, as is evident from the pv diagrams we show in Fig. 2. This system is confined to within $\pm 3''$ of the center and distinctly different from the material within the ‘main’ bar, where the velocity changes much more slowly, which is seen in panel (a), a cut along the major bar axis.

Table 2. Summary of the interferometric observations of NGC 7479

Line, ν (GHz)	Date	Field Center	uv-Coverage	Prim. Beam	Syn. Beam	Conf. ^{a)}	T_{sys}	Noise ^{b)}
$^{12}\text{CO}(1 \rightarrow 0)$	2/96	23 ^h 02 ^m 26.4 ^s	6k λ – 46k λ	63''	4''.6 \times 4''.25	L,E	$\sim 500\text{K}$	85 mK
115.271	4/96	12 $^{\circ}$ 03' 10.6''	(15m – 119m)		PA –9 $^{\circ}$			
$^{13}\text{CO}(1 \rightarrow 0)$	2/96, 3/96		5.7k λ – 44k λ	66''	4''.9 \times 4''.05	L,E	$\sim 300\text{K}$	23 mK
110.201	5/96, 6/96		(15m – 119m)		PA –45 $^{\circ}$			
HCN($1 \rightarrow 0$)	2/96		4.4k λ – 35k λ	80''	7''.2 \times 5''.2	L,E	$\sim 300\text{K}$	12 mK
88.632	5/96		(15m – 119m)		PA –49 $^{\circ}$			

a): The array configurations we used at OVRO are labelled L (low resolution) and E (equatorial)

b): This is the rms noise per channel (20 km s^{-1} for CO, 40 km s^{-1} for HCN). On a mJy beam^{-1} -scale, the values correspond to 18 mJy beam^{-1} (^{12}CO), and 5 mJy beam^{-1} (^{13}CO and HCN).

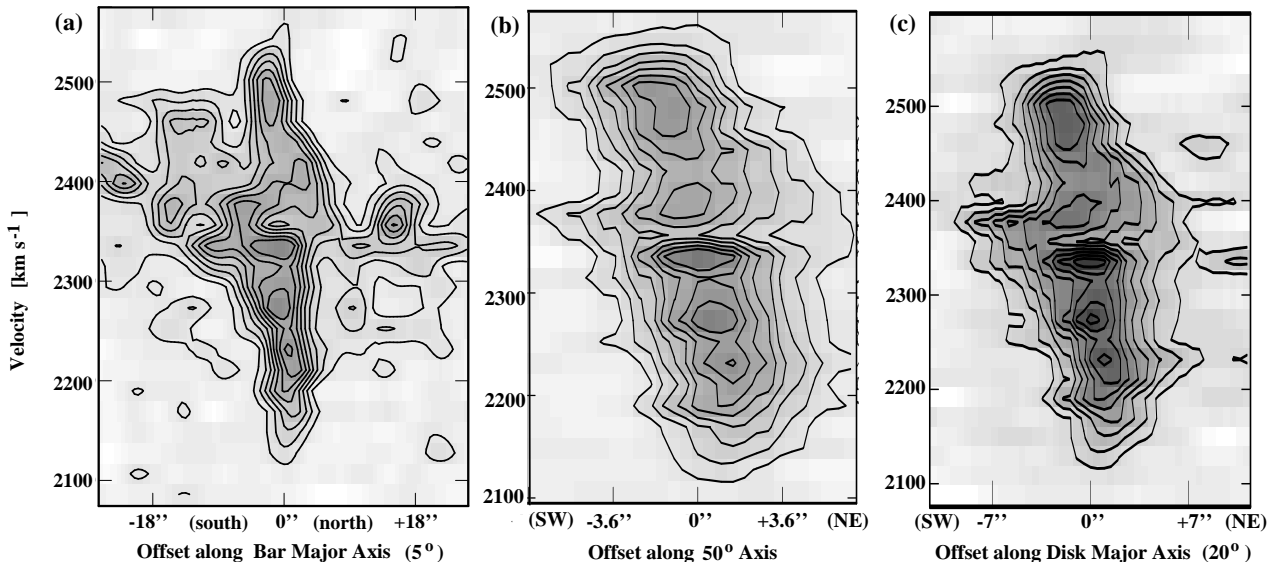


Fig. 2. a) Position velocity diagram along the major axis of the ^{12}CO bar (position angle 5° (north-to-east)). Thus, the bar is oriented very close to the north-south direction. b) Position velocity diagram along the axis with position angle 50° (i.e. 45° relative to the bar major axis). This is the angle that best shows the central rapidly rotating structure. c) Position velocity diagram along the disk major axis, at a position angle of 25° (i.e. 20° relative to the bar major axis). For all panels, the contours are multiples of 2σ (0.17K or 36 mJy beam^{-1}).

The central rapidly rotating structure is most easily seen at a position angle close to 45° (panel (b)). While there is a central peak (at $v_{\text{LSR}} = 2330\text{ km s}^{-1}$), this peak does not dominate the emission: other features at velocities ranging from 2200 km s^{-1} to 2500 km s^{-1} are almost as strong and spatially separated by $1''$ – $2''$.

A high velocity system like this is a signature feature of many barred galaxies. It has been used by Binney et al. (1991) to argue the presence of a central bar in our Galaxy. The orbits of the gas that can cause this feature have been modelled by e.g. García-Burillo & Guelin (1995) for the case of the weakly barred edge-on galaxy NGC 891. The structure found in NGC 7479 (already noted by Laine et al. 1999) also greatly resembles the system seen in

UGC 2855, a strongly barred galaxy where, in contrast to NGC 7479, quiescent conditions are found for the gas along the bar (Hüttemeister et al. 1999). As in UGC 2855, the central high velocity system in NGC 7479 can be interpreted as a clumpy tilted ring or torus close to the ILR (which we would then place at $2''$ – $3''$ from the nucleus), as a fragmented, tilted, rotating nuclear disk that is freely fed from material inflowing through the bar without being stopped at an ILR, or even as a dynamically decoupled inner bar, as tentatively suggested by Baker (2000).

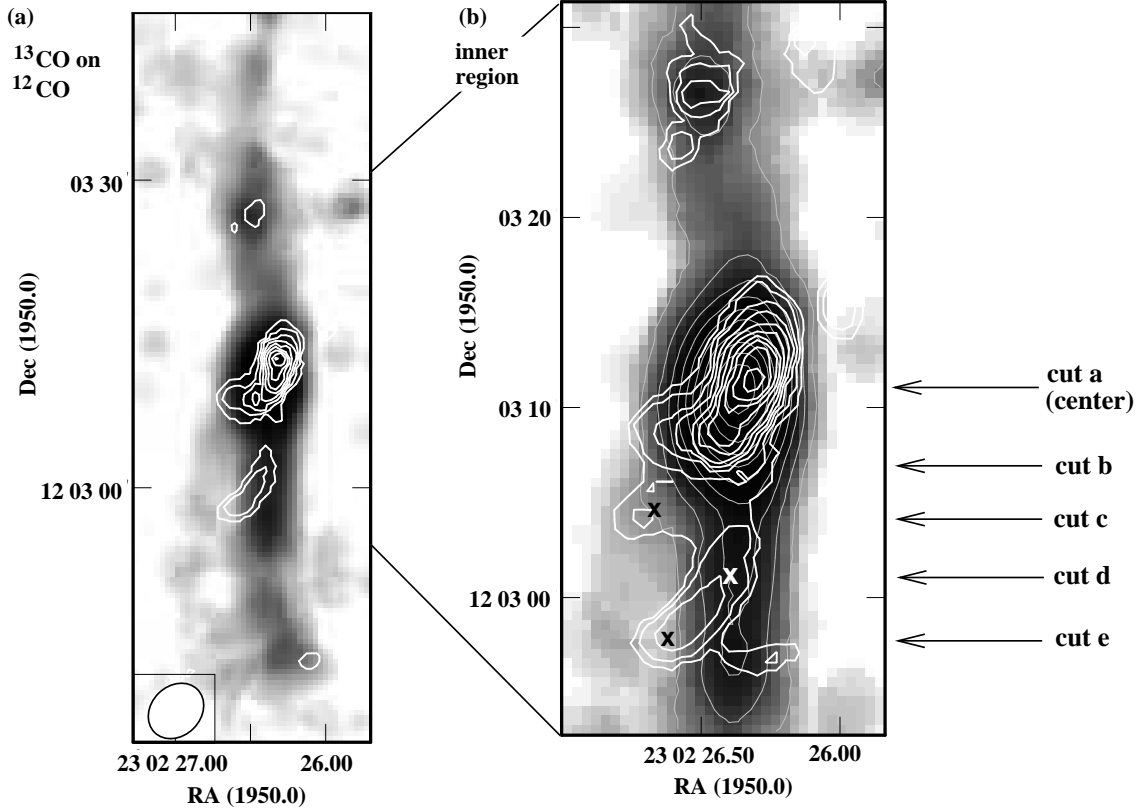


Fig. 3. The distribution of the ^{13}CO emission (contours) superposed on the ^{12}CO intensity map (greyscale). a) Intensity integrated over the full velocity width in the center, i.e. 400 km s^{-1} . The contours start at 1.4 K km s^{-1} ($0.3 \text{ Jy beam}^{-1} \text{ km s}^{-1}$ or 1.5σ for a width of 80 km s^{-1}) and are spaced by 1.85 K km s^{-1} . b) The inner region of the bar, integrated over 200 km s^{-1} only to bring out emission from narrow lines. The contours start at 0.9 K km s^{-1} ($0.2 \text{ Jy beam}^{-1} \text{ km s}^{-1}$, 1.5σ for a velocity width of 40 km s^{-1}) with a spacing of 1.35 K km s^{-1} . The crosses mark the positions for which spectra are shown in Fig. 5. Thin gray contours refer to ^{12}CO . The arrows mark the positions of the intensity cuts in Fig. 9.

3.1.2. Comparison with Prior ^{12}CO Maps

The general morphological structure and velocity field of our map are in excellent agreement with the results reported by Laine et al. (1999). However, the ^{12}CO emission in our map is a continuous bar structure, while the structure seen by Laine et al. breaks up into separate clumps away from the central condensation, a large part of the body of the bar being devoid of emission. As can be expected if the two maps are consistent, the position of these clumps is in exact agreement with the peaks we see embedded in more extended emission.

Comparing the total fluxes contained in the maps, we find that our flux is higher by a factor of 1.45 than that seen by Laine et al. This discrepancy is caused by our map being more sensitive by a factor of ~ 2 , due to a larger beam size combined with a slightly longer integration time. Thus, the larger East-West diameter of the bar seen in our map and its continuity are not artifacts of

smearing by lower resolution, but real effects: Our map picks up an additional, more smoothly distributed gas component traced by ^{12}CO . We can compare our total flux to the flux seen in the single dish map of Sempere et al. (1995), which covered a larger area than our map. However, $\sim 80\%$ of the flux is contained in the region of the OVRO primary beam. We find that we recover more than 90% of this flux, which is consistent with Laine et al., who report recovering 60% of the single dish flux in their less sensitive map. Thus, *there is very little, if any, missing flux in our ^{12}CO map* and we can analyse the complete molecular distribution as traced by ^{12}CO at high resolution. *This complete recovery of flux is the main distinguishing feature between our ^{12}CO map and the interferometric maps published previously, both by Laine et al. and earlier by Quillen et al. (1995).*

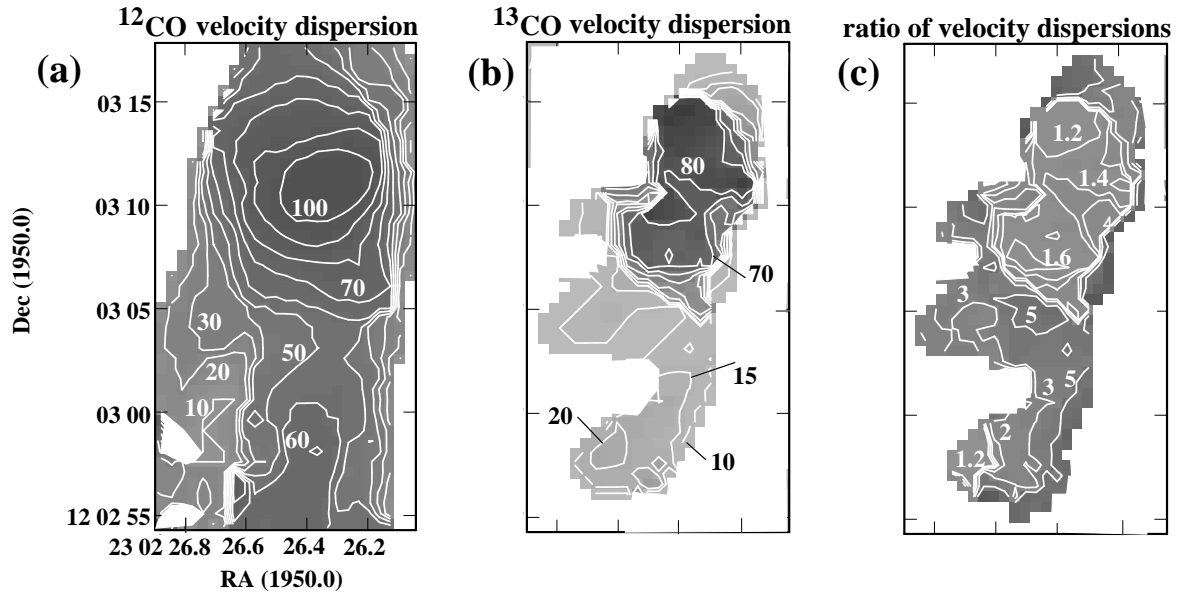


Fig. 4. Maps of the one-dimensional velocity dispersion in the inner region where continuous ^{13}CO emission is detected. a) ^{12}CO . The contours range from 10 km s^{-1} to 100 km s^{-1} in steps of 10 km s^{-1} . b) ^{13}CO . The contour levels are at 10 km s^{-1} , 15 km s^{-1} and then range from 20 km s^{-1} to 80 km s^{-1} in steps of 10 km s^{-1} . c) Ratio of the ^{12}CO velocity dispersion to the ^{13}CO velocity dispersion. The contours label ratios of 1.2, 1.4, 1.6, 2, 3 and 5.

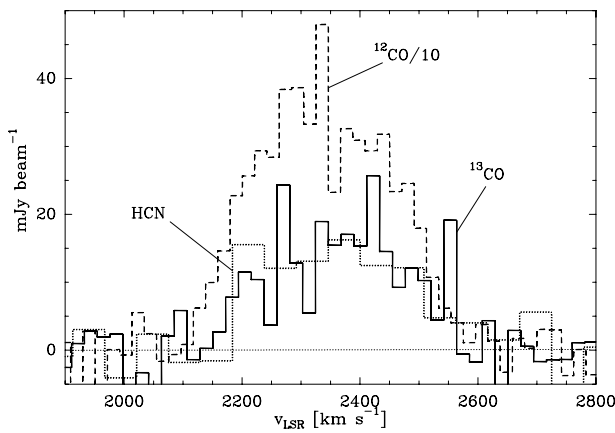


Fig. 5. Spectra of the central position (taken at the position with the highest ^{12}CO intensity, i.e. $\alpha = 23^{\text{h}} 02^{\text{m}} 26.37^{\text{s}}$ and $\delta = 12^{\circ} 03' 11.6''$). The dashed line is ^{12}CO divided by 10 for better comparability, the solid line is ^{13}CO and the dotted line HCN. All three spectra above correspond to a region with the $7''2 \times 5''2$ size of the HCN beam; the ^{12}CO and ^{13}CO data were smoothed to the same beamsize as the HCN data. 20 mJy beam^{-1} correspond to 73 mK (HCN) or 44 mK (^{12}CO).

3.2. Distribution of ^{13}CO and HCN

Since ^{13}CO and HCN usually originate from regions that are more compact and confined than ^{12}CO emitting gas, we consider it very likely that we also recover the entire

flux for those molecules, being limited only by sensitivity, not by missing zero-spacings in the interferometer map.

The distribution of the ^{13}CO emission is presented in Fig. 3. While Fig. 3a gives the moment 0 map for the full central velocity of 400 km s^{-1} (see Fig. 5), panel b is integrated over only 200 km s^{-1} , so that very narrow lines are not lost in the noise. Now, a connection between the central distribution and the southern feature becomes apparent. The example spectra shown in Fig. 6 demonstrate the narrowness of these lines. The total ^{13}CO flux we detect is $\sim 9 \text{ Jy km s}^{-1}$.

The ^{13}CO emission is distributed very differently from the ^{12}CO . The central ^{13}CO peak is significantly offset to the north-west from the ^{12}CO peak (by $2''$ or 320 pc in linear size).

While the ^{12}CO distribution in the central concentration and south of the center along the bar runs almost exactly north-south, the central ^{13}CO distribution is best described as extending along a position angle of -30° , with a curvature toward the south-east (Fig 3). The deviation between the ^{12}CO and ^{13}CO morphology is even clearer in the southern ^{13}CO extension at offsets $7''$ to $15''$ to the south along the bar.

No ^{13}CO is seen at corresponding offset along in the northern part of the bar.

The weak feature offset $\sim 20''$ to the north, close to the bar end, has no southern counterpart, but is coincident with a peak in the ^{12}CO distribution and thus likely to be real. Further peaks at the bar ends are not detected with at a sufficient confidence level, since these regions are

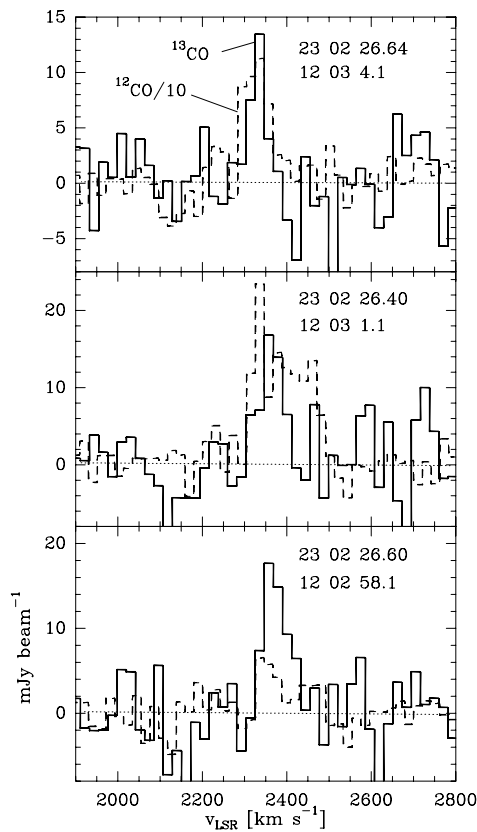


Fig. 6. Offset spectra for ^{12}CO divided by 10 (dashed) and ^{13}CO (solid). The positions are marked in Fig 3 and correspond to regions with the size of the beam of the CO observations ($\sim 5'' \times 4''$, see Table 2). For the ^{12}CO beam used here, 20 mJy beam $^{-1}$ correspond to 97 mK.

close to the edges of our primary beam, and any emission may be affected by the fall-off in sensitivity as well as sidelobes of the central peak. One might expect to recover ^{13}CO again close to the bar edges, due to the crowding of elliptical (x_1) streamlines, resulting in increased cloud collisions and the formation of dense shocked gas. Further high sensitivity studies are needed to clarify this point.

Still, very dramatic changes in the ^{12}CO to ^{13}CO line intensity ratio are evident, both in the central region and along the bar. These changes, which are indicators of changing gas properties, will be discussed in detail in the subsequent section.

HCN is clearly detected only in the very center of the ^{12}CO distribution (Fig. 7). It is unresolved and its position is consistent with the ^{12}CO peak, i.e. offset from the maximum ^{13}CO intensity. The total HCN flux in this central structure is 1.6 Jy kms.

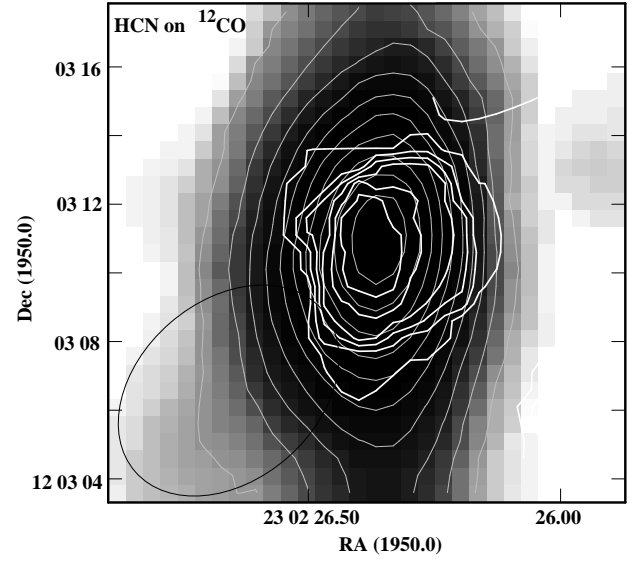


Fig. 7. The total integrated intensity of HCN, superposed on ^{12}CO (grayscale and thin grey contours). The HCN contour levels start at 1 K km s $^{-1}$ (0.42 Jy beam $^{-1}$ km s $^{-1}$ or 1.5σ) and increase in 2σ steps. The ellipse in the lower left corner denotes the HCN beam and demonstrates that the HCN emission is not resolved.

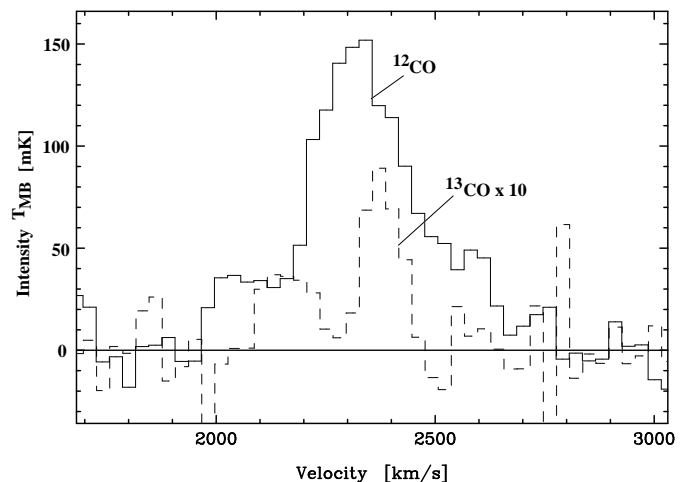


Fig. 8. Single dish observations of ^{12}CO and ^{13}CO taken with the OSO 20 m telescope. The beamsize is $33''$, the intensity scale is T_{MB} (main beam efficiency $\eta_{\text{MB}} = 0.5$).

3.3. Line intensity ratios

We present line intensity ratios taken between ^{12}CO and ^{13}CO ($\mathcal{R}_{12/13}$) in different positions and over different areas in Table 3. In this table, we have computed $\mathcal{R}_{12/13}$ and its errors individually for the peak intensity, the integrated

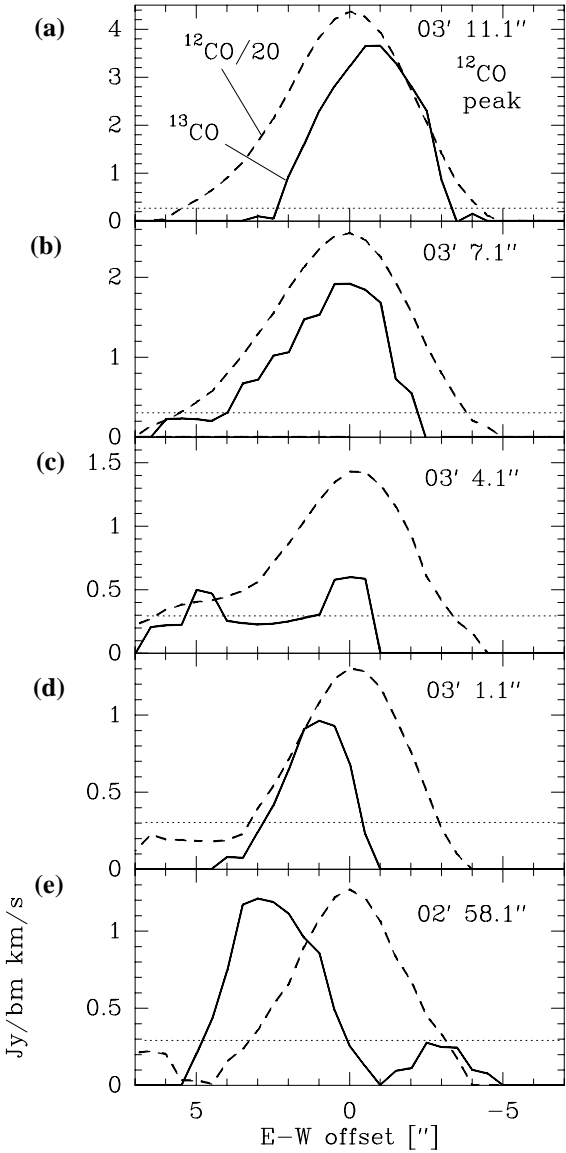


Fig. 9. East-West cuts in integrated intensity through the bar at the positions marked in Fig. 3. The north-south width of the cuts correspond to the $4'' - 5''$ beamwidth of the CO observations. Solid lines are ^{13}CO , dashed lines are ^{12}CO divided by 20. The integrated intensities refer to a velocity range of 450 km s^{-1} , i.e. the full range where ^{12}CO emission is found. The thin dashed line is the 2σ limit for ^{13}CO and a velocity width (FWHM) of 40 km s^{-1} , i.e. the typical width of off-center ^{13}CO lines. Thus lower ^{13}CO intensities have no meaning. All offsets are relative to the right ascension of the ^{12}CO peak position. $1 \text{ Jy beam}^{-1} \text{ km s}^{-1}$ corresponds to 4.8 K km s^{-1} .

intensity as measured within the velocity window where ^{13}CO is detected and the velocity range within which we find ^{12}CO emission. The respective velocity ranges are given along with the values of $\mathcal{R}_{12/13}$. Again, it is obvious that the ^{13}CO line usually is narrower than the ^{12}CO line, especially at and close to the ^{12}CO peak region along the bar. Moving away from this peak, the ^{12}CO linewidth drops and approaches that of ^{13}CO (see the dispersion maps for ^{12}CO and ^{13}CO (Fig. 4) and the spectra displayed in Fig. 6). Especially from Fig. 4c), which displays the ratio of the ^{12}CO and the ^{13}CO velocity dispersion, it is clear that the velocity dispersion of ^{13}CO always is smaller than the velocity dispersion of ^{13}CO . The dispersions are similar (ratio < 2) in the central $\sim 10''$, where the ^{13}CO line is fairly wide ($\delta v_{\text{mom}} \approx 60 - 80 \text{ km s}^{-1}$) and in the southern ^{13}CO concentration, where the ^{12}CO transition becomes narrow ($\delta v_{\text{mom}} \approx 10 - 30 \text{ km s}^{-1}$). The ratio of the dispersion is high (3 – 6) close to the ^{12}CO peak region along the bar, where the ^{12}CO line is wide, while the ^{13}CO line is narrow.

The global $^{12}\text{CO}/^{13}\text{CO}$ intensity ratio, i.e. the ratio we find when comparing the total fluxes for the entire map, is quite high at ~ 40 , certainly much higher than what is typical for gas in galactic disks or even ‘normal’ galactic nuclei (see Table 3 for typical values). It is very unlikely that this ratio is an artifact of missing flux, since almost all flux in ^{12}CO is seen and we do not expect to miss more flux in the more compactly distributed ^{13}CO . However, lack of sensitivity to ^{13}CO is a concern.

To evaluate the possible magnitude of this effect, we assume that ^{13}CO emission in a velocity range of 200 km s^{-1} is present at the 2σ level in all places where ^{12}CO is detected and we do not find ^{13}CO . This (unlikely) scenario would result in an additional flux of $10.8 \text{ Jy km s}^{-1}$, i.e. roughly double our ^{13}CO flux and bring the global ratio down from 42 to 19, which we thus regard as a firm lower limit. We have also estimated the global value of $\mathcal{R}_{12/13}$ using the global spectra of ^{12}CO and ^{13}CO , i.e. spectra constructed for the entire spatial extent of ^{12}CO emission. Here, ^{13}CO is only tentatively detected. Using a 3σ limit and a velocity range of 450 km s^{-1} , we obtain a ratio of $\mathcal{R}_{12/13} \geq 30$, in full agreement with the ratio determined using integrated fluxes.

In the central condensation, the variation in $\mathcal{R}_{12/13}$ goes along with the morphological shift described above. $\mathcal{R}_{12/13}$ ranges from ~ 10 close to the ^{13}CO ‘ridge’ to ~ 30 at distances of $5''$ or more from it. The average ratio over the central condensation is fully consistent with the ratio determined from the single dish spectra taken toward the central position (Fig. 8). Since we expect the central condensation to dominate the single dish flux in the central $33''$, this result confirms our prior conclusion that there is no missing flux in the interferometry maps.

The even more drastic variation of $\mathcal{R}_{12/13}$ in the bar is evident from both Table 3 and Fig. 9. The latter presents another easy way of visualizing the changing line ratios.

Table 3. $^{12}\text{CO}/^{13}\text{CO}$ 1 → 0 line ratios ($\mathcal{R}_{12/13}$) for NGC 7479 and typical galactic ratios. The ‘cuts’ refer to Fig. 9. Individual random errors are given in parentheses. The error in the scaling of all ratios due to calibration uncertainties is estimated to be $\sim 20\%$.

Position	Peak Ratio	Integrated Ratios		
		Region of ^{13}CO line	Range ^{a)} [km s $^{-1}$]	Region of ^{12}CO line
global (bar and center)	–	≤ 42 ^{b)}		
^{12}CO maximum intensity	27(7)	19(2)	320	25(3) 440
^{13}CO maximum intensity	16(6)	18(2)	320	23(3) 440
cent. cond. (average)	22(8)	22(4)	400	23(4) 440
central region (OSO)	19(4)	21(3)	390	28(4) 500
cent. cond. (individual)		10 – 30 ^{c)}		
Peak of cut b	27(9)	25(5)	220	29(7) 400
^{12}CO peak of cut c	19(5)	17(4)	60	40(15) 340
^{13}CO peak of cut c (east)	6.4(1.6)	10(2)	105	14(4) 200
^{12}CO peak of cut d	11(3)	10(2)	80	28(6) 200
^{13}CO peak of cut d	4.7(2.2)	5.1(2.4)	80	17(3) 180
^{12}CO peak of cut e	24(10)	22(5)	100	73(37) 260
^{13}CO peak of cut e	3.5(1.4)	3.5(0.6)	100	3.5(0.6) 100
northern ^{13}CO peak	12(4)	10(2)	140	14(3) 220
no ^{13}CO detections:				
offset +10 $''$ along bar	–	–	–	>15 ^{d)} 220
offset -17 $''$ along bar	–	–	–	>25 ^{d)} 280
offset -21 $''$ along bar	–	–	–	>25 ^{d)} 160
galactic disk	~ 6 ^{e)}			
centers of ‘normal’ galaxies	13 ± 6 ^{f)}			

a) The velocity range gives the region where the ^{12}CO or ^{13}CO line is detected above the noise.

b) Under extreme assumptions, this can be brought down to 20 (see text)

c) Range encountered in the central 10 $''$, both in peak and integrated ratios

d) 3σ limit calculated over the range where ^{12}CO is visible.

e) Polk et al. 1988; f) Aalto et al. 1995

It shows cuts in integrated intensities (over a range of 450 km s $^{-1}$, chosen to include all ^{12}CO emission) along the bar minor axis at a number of offsets. Here, we focus on the southern ^{13}CO extension. As the ^{13}CO emission shifts eastward from ^{12}CO when we move south along the bar, the line ratios change from values around 25 in the central condensation to ~ 40 (integrated intensity) at the ^{12}CO maximum along the bar. The ratios calculated using the peak flux and the velocity range of the ^{13}CO emission are often smaller than the $\mathcal{R}_{12/13}$ referring to the velocity range of the ^{12}CO line since in many places the ^{13}CO lines are narrower than the ^{12}CO lines. At the declination of the maximum of the southern ^{13}CO distribution, $\mathcal{R}_{12/13}$ drops from 73 ± 37 to 3.5 ± 0.6 (integrated) or 24 ± 10 to 3.5 ± 1.4 (peak) within 5 $''$! Interestingly, in this position, off the ^{12}CO peak, the widths of the two transitions are identical. These values of $\mathcal{R}_{12/13}$ are put into perspective by noting that $\mathcal{R}_{12/13}$ of 6 – 7 is typical for global ratios in galactic spiral arms (Polk et al. 1988), which might already include the contribution of some diffuse gas, while Galactic GMCs typically show $\mathcal{R}_{12/13}$ values of 3–5. An $\mathcal{R}_{12/13}$ exceeding 30 is only seen in a few luminous mergers (Casoli et al. 1992, Aalto et al. 1991).

The central gas surface density of NGC 7479 ($\sim 2000 M_{\odot} \text{pc}^{-2}$, using the ‘standard’ CO to N(H₂) conversion factor for comparison purposes only, see discussion below) is high enough to place the nuclear region in the range of IR-bright starburst galaxies (Scoville 1991), even though ultraluminous IR galaxies (ULIRGs) can have core gas surface densities up to an order of magnitude higher (e.g. Bryant & Scoville 1999, who obtained exceeding $20000 M_{\odot} \text{pc}^{-2}$ for NGC 2623, Mrk 231 and NGC 6240, assuming a standard conversion factor). However, the gas surface density in the bar of NGC 7479, where the most extreme values of $\mathcal{R}_{12/13}$ are reached, is far smaller than in luminous starbursts, pointing to a different dominant mechanism accounting for the high value of $\mathcal{R}_{12/13}$.

The large changes of $\mathcal{R}_{12/13}$ have to indicate a very significant change in the properties of the emitting gas, scenarios for which will be discussed below

HCN 1 → 0 emission is detected only in the nucleus, with a $^{12}\text{CO}/\text{HCN}$ line ratio ≈ 20 .

4. Discussion

4.1. Gas Masses Based on CO Isotopomers

The total flux in our map *would* correspond to an H_2 mass of $4 \cdot 10^9 M_\odot$ if the ‘standard’ CO to $N(H_2)$ conversion factor ($SCF = X_{CO} = 2.3 \cdot 10^{20} \text{ cm}^{-2} (\text{K km s}^{-1})^{-1}$, Strong et al. 1988) were applicable, which is, however, not the case (see discussion below). Instead of giving more masses based on the standard conversion factor, which are unlikely to be very meaningful, we compare the ‘standard’ mass derived from ^{12}CO to masses from ^{13}CO obtained with the simple LTE assumptions of optically thin emission and a kinetic gas temperature of 20 K. *Globally*, i.e. avaraged over the entire map, the ^{13}CO -derived mass is a factor of 16 – 27 (for $^{12}\text{CO}/^{13}\text{CO}$ abundance ratios between 30 and 50) lower than the SCF mass. If the upper limit for the ^{13}CO total flux (see below) is taken, the discrepancy decreases to 8 – 13, still remaining very substantial. A mass discrepancy of ~ 10 is also derived for the central condensation. In ^{12}CO peaks along the bar, the disagreement between the SCF and the ^{13}CO LTE mass reaches values exceeding 30, while in the ^{13}CO maximum in the southern bar, it comes down to ~ 2 . Of course, these varying mass discrepancies simply reflect the changing line intensity ratios discussed above.

The SCF mass still exceeds the ^{13}CO LTE mass by a factor 2 – 10 if the kinetic gas temperature is raised from 20 K to 100 K for the ^{13}CO - based estimate. Only in the ^{13}CO peak in the bar south of the central condensation the SCF mass drops to about half the ^{13}CO LTE mass under these conditions, which are, of course, not realistic for a ^{13}CO condensation, presumably consisting of dense gas. However, it seems that the SCF might be correct in this (and only in this) location, which has almost exactly the $^{12}\text{CO}/^{13}\text{CO}$ line ratio found in Galactic GMCs. This can be considered as a way to confirm the SCF for a normal spiral environment.

Of course, assuming LTE conditions when deriving $N(H_2)$ from ^{13}CO could underestimate the true $N(H_2)$ when non-LTE conditions apply. Padoan et al. (2000) find a discrepancy of a factor 1.3 – 7 between ‘LTE masses’ and ‘true’ masses in their cloud models. This discrepancy is smaller than the difference between the ^{13}CO LTE masses and the SCF masses we find both for the gas in the center and, even more pronounced, for the gas in ^{12}CO peaks along the bar away from center. Still, the ^{13}CO masses derived for LTE should be considered as a lower limit to the real mass, while the SCF masses are upper limits.

Simple non-LTE radiative transfer calculations (using the Large Velocity Gradient (LVG) assumption) reproduce the results of Padoan et al. to within roughly a factor of two and can thus serve as a guide to possible scenarios. These calculations show that the ^{12}CO -to- H_2 conversion factor can be brought down significantly (by a factor of ~ 6) in low density gas ($n(H_2) \gtrsim 100 \text{ cm}^{-3}$). Then, high $^{12}\text{CO}/^{13}\text{CO}$ 1 \rightarrow 0 line intensity ratios of 20 – 30 are

predicted. Thus, this scenario points to the presence of ‘diffuse’ gas, discussed in detail in the next section.

When the density is reduced even further, in the LVG models the ^{12}CO -to- H_2 conversion factor rises again. The SCF can be recovered for a H_2 density of $\sim 10 \text{ cm}^{-3}$, while $\mathcal{R}_{12/13}$ remains high. We consider these extremely low densities required for the bulk of the gas unlikely for the following reasons: To reach a column density that is sufficient to ensure shielding of the molecules against UV radiation and to be consistent with the observed brightness of the lines, even for an extreme and very unlikely beam filling factor of unity, the models require an unrealistically low velocity dispersion for a given pathlength ($\leq 0.05 \text{ km s}^{-1} \text{ pc}^{-1}$). This is in contradiction to the expectation that diffuse gas should be characterized by a large velocity dispersion (see below). Another argument against extremely low density gas is the expected very low $^{12}\text{CO}(2 \rightarrow 1)/(1 \rightarrow 0)$ line intensity ratio (< 0.3), in contradiction to single-dish (Sempere et al. 1995) and recent interferometric observations of $^{12}\text{CO}(2 \rightarrow 1)$ (Baker 2000).

4.2. Physical Conditions – Diffuse Molecular Gas

In this section, we present simple scenarios that might explain the variations in $\mathcal{R}_{12/13}$. The key component of these scenarios is the presence of a *diffuse or ‘intercloud’ molecular medium (ICM)*. This medium consists of low density ($n \lesssim 10^3 \text{ cm}^{-3}$), gravitationally unbound, molecular gas. For a given column density, N , the ^{13}CO 1 \rightarrow 0 line emission from gravitationally unbound gas will be weaker than that from self-gravitating clouds, because the velocity dispersion, δv , is higher for unbound material and thus $N/\delta v$ is lower for the unbound gas. A low $N/\delta v$ results in a low optical depth and, in low-density gas, also results in a low excitation temperature of the transition because of reduced radiative trapping. Hence, the ICM will be difficult to detect in the ^{13}CO 1 \rightarrow 0 line. One may see the ICM as somewhat analogous to high latitude molecular clouds detected in the disk of our Galaxy. These are also low density structures which, unlike most of the disk molecular clouds, are not in virial equilibrium.

While, under these conditions, ^{13}CO is optically thin and subthermal, ^{12}CO reaches a moderate optical depth close to unity. Thus, ^{12}CO still radiates efficiently (and is self-shielding) while the ^{13}CO intensity falls off. This moderate optical depth of the ^{12}CO 1 \rightarrow 0 line is the main reason why *the ‘standard’ X_{CO} conversion factor cannot be applied to regions where a significant amount of diffuse gas is found*: the gas is neither optically thick nor virialized and the ‘standard’ X_{CO} overestimates the molecular gas mass by up to an order of magnitude. This situation is encountered, e.g., in our Galactic center (Dahmen et al. 1998).

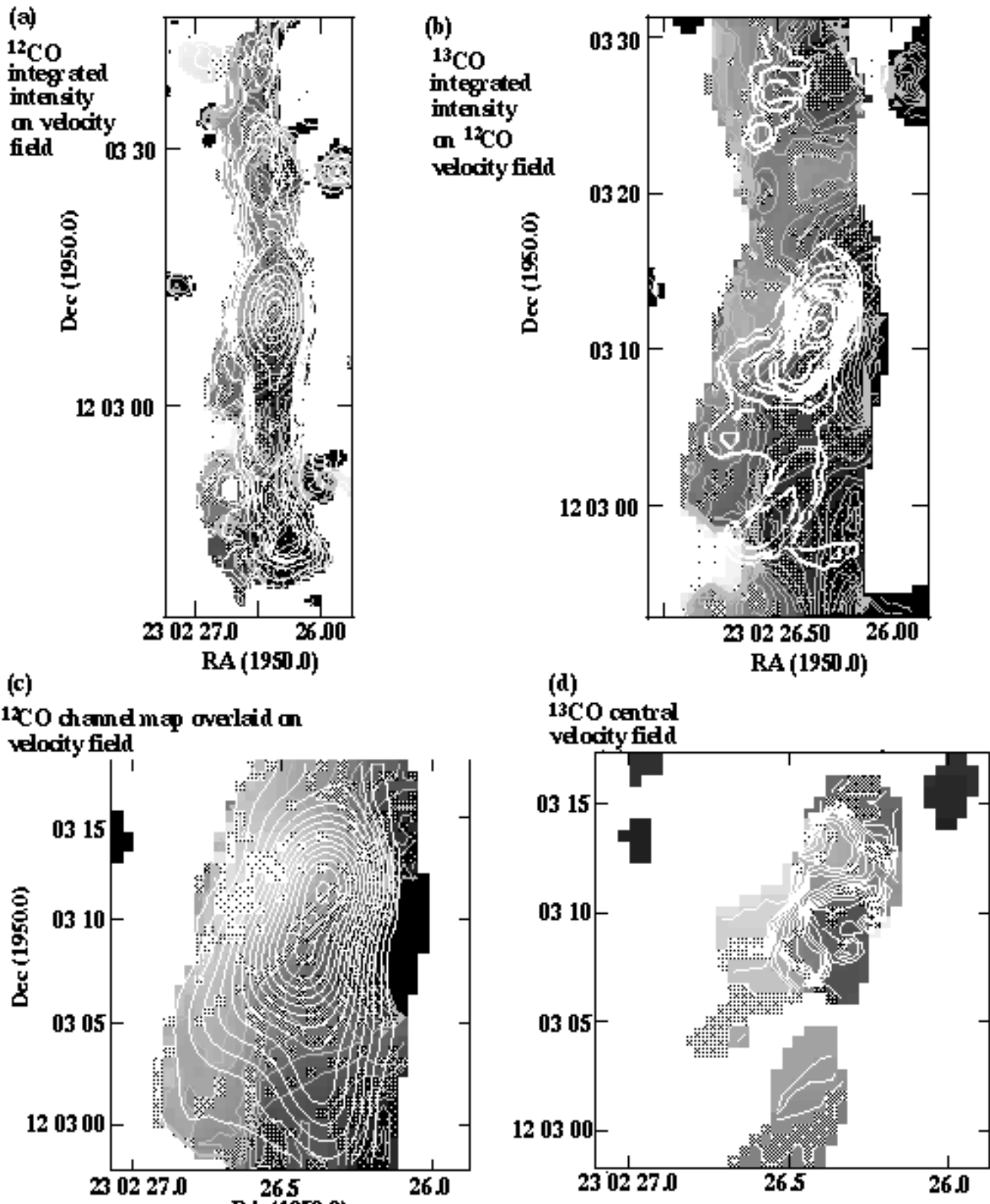


Fig. 10. (a) The integrated ^{12}CO intensity (white contours) superposed on the velocity field derived from ^{12}CO (grayscale and thin gray contours). The velocity contours range from 2280 km s^{-1} to 2440 km s^{-1} and increase by 10 km s^{-1} . (b) The integrated ^{13}CO intensity (white contours) superposed on the velocity field from panel (a). The velocity contours are the same as in panel (a) and thus facilitate a direct comparison of the two panels. (c): ^{12}CO channel map for the velocity range 2280 km s^{-1} – 2340 km s^{-1} (white contours) overlaid on the ^{12}CO velocity field in the central part of the bar (grayscale and gray contours). The intensity contours are multiples of 2σ (5.9 K km s^{-1} ($1.24 \text{ Jy beam}^{-1} \text{ km s}^{-1}$ or 2σ)). The velocity contours are the same as in panel (a). In grayscale, dark corresponds to

4.2.1. The Bar – Outside the Central 10'' Diameter

The large variations in $\mathcal{R}_{12/13}$ along the bar, with values ranging from 5 to > 40 (and even 73 in one extreme case) is best explained by the presence of a large amount of diffuse (thin, warm, unbound) ICM gas which dominates the ^{12}CO $1 \rightarrow 0$ emission and is very distinctly different from the dense molecular clouds preferentially detected by ^{13}CO . In the southern part of the bar, where ^{13}CO is detected, the difference in linewidth is most dramatic close to the ^{12}CO maxima. Here, the ^{12}CO lines have a width of $\sim 200 \text{ km s}^{-1}$, compared to $\sim 50 \text{ km s}^{-1}$ for ^{13}CO . This explains the significant difference in $\mathcal{R}_{12/13}$ depending on whether integrated or peak intensities are used (Table 3). The large linewidths of the ^{12}CO spectra suggest large velocity dispersions at the ^{12}CO maxima along the bar. This provides a strong argument in favour of a diffuse medium contrary to $[^{12}\text{CO}]/[^{13}\text{CO}]$ abundance variations. While in a ‘standard’ ^{12}CO emitting ISM, i.e. a medium where low J ^{12}CO lines are optically thick, the $[^{12}\text{CO}]/[^{13}\text{CO}]$ abundance ratio is not traced by changes in $\mathcal{R}_{12/13}$, a change in the ^{13}CO abundance itself could contribute to changes in $\mathcal{R}_{12/13}$. However, if such a variation reflects changes in $[^{12}\text{C}]/[^{13}\text{C}]$ with galactocentric radius, it should not exceed a factor of two (Wilson & Matteucci 1992, Langer & Penzias 1990). Even a gradient this small and insufficient to explain the observed changes in $\mathcal{R}_{12/13}$ is almost impossible to maintain in the bar due to efficient mixing (see e.g. Friedli et al. 1994 for model calculations, Martin & Roy 1994 and Zaritsky et al. 1994 for empirical studies). Thus, we consider diffuse gas to provide the only viable explanation for the large variations in $\mathcal{R}_{12/13}$ we find along the bar of NGC 7479.

Of course, ^{13}CO may be selectively photodissociated in the diffuse medium and thus really be underabundant, since it is not self-shielding. However, the efficiency of this mechanism also relies on the diffuse nature of the gas.

According to the single dish map of Sempere et al. (1995), the $^{12}\text{CO}(2 \rightarrow 1)/(1 \rightarrow 0)$ ratio along the bar is ~ 0.6 . This is, of course, a global value which is likely to vary at higher resolution. It is compatible with cold gas at moderate density ($10^3 - 10^4 \text{ cm}^{-3}$) or warm, thin gas (density a few 100 cm^{-3}). Given the evidence discussed above, we obviously favour the latter explanation for this line ratio.

The fact that the ^{13}CO intensity maximum is clearly offset along the bar minor axis from the ^{12}CO maximum in the southern bar indicates that ^{13}CO traces a largely different component. The relation of the two tracers to dust, shocks and star formation will be discussed further in Section 4.3.

4.2.2. The Inner Region – Inside the Central 10''

At first glance, the situation in the center of NGC 7479 might be taken to argue against the ICM scenario out-

lined above, since the HCN is coincident with the ^{12}CO maximum and offset from ^{13}CO . A situation like this was sometimes seen as suggesting abundance changes for the CO isotopomers (e.g. Casoli et al. 1992), since HCN requires high gas densities of at least 10^4 cm^{-3} to be significantly excited and may be identified with the region where most of the mass resides. In a turbulent environment like the nuclear region of NGC 7479, we consider the alternative *explanation of a kinetic temperature gradient between the ^{13}CO and HCN peaks* to be more likely. For the high gas densities we expect in the central region (i.e. $n(\text{H}_2) > 10^4 \text{ cm}^{-3}$), the higher kinetic temperature would occur at the HCN peak rather than the ^{13}CO peak because the brightness of the ^{13}CO $1 \rightarrow 0$ line is a decreasing function of kinetic temperature (for temperatures above 8 K in the LTE, optically thin limit).

The HCN molecule has a high dipole moment and is thus much more sensitive to density variations than ^{12}CO and ^{13}CO . Thus the HCN peak is not expected to coincide with the ^{13}CO peak if the latter is at lower densities than the HCN $1 \rightarrow 0$ critical density. This is true even if the HCN $1 \rightarrow 0$ transition is optically thin, due to the spreading of the molecules over many rotational levels that occurs at high densities (i.e. 10^6 cm^{-3} for HCN) because of the high collision rates at these densities.

We can give an order-of-magnitude estimate of the gas density that is likely to occur at the HCN peak: Having the bulk of the gas in the central beam at densities of $\sim 10^6 \text{ cm}^{-3}$ requires a very low volume filling factor of $\lesssim 10^{-4}$, which seems unlikely in the center of a galaxy undergoing a mild starburst. Also, very high densities suggest a velocity dispersion per pathlength that is too high to be realistic (several $100 \text{ km s}^{-1} \text{ pc}^{-1}$). If, on the other hand, the density was low enough for HCN to be subthermally excited, the HCN $1 \rightarrow 0$ line would be optically thick, because the molecules would pile up in the $J = 0$ level. However, in this case (at peak densities of $\sim 10^4 \text{ cm}^{-3}$) we would expect the emission to be more widespread. Low densities close to 10^3 cm^{-3} lead to very subthermal conditions and very weak HCN $1 \rightarrow 0$ emission. Thus, we consider $\sim 10^5 \text{ cm}^{-3}$ to be a reasonable density at the HCN peak.

In summary, since the HCN distribution is confined closely to the ^{12}CO peak, we expect this region to also be a peak in density (but not necessarily in column density), in addition to being a peak in T_{kin} . In contrast, the ^{13}CO $1 \rightarrow 0$ emission will preferentially trace cool and/or lower density gas.

A kinetic temperature gradient was also used to explain the different spatial extents of the $^{13}\text{CO}(3 \rightarrow 2)$ and HCN emission in NGC 253 (Wall et al. 1991). The kinetic temperature gradient in NGC 7479 leads to the prediction that the $^{13}\text{CO}(2 \rightarrow 1)/(1 \rightarrow 0)$ ratio should be higher in the HCN peak than in the ^{13}CO peak, as is seen in the nucleus of IC 694 in the Arp 299 merger (Aalto et al. 1997b). It also means that the nuclear $^{12}\text{CO}(2 \rightarrow 1)/^{12}\text{CO}(1 \rightarrow 0)$ ratio is

expected to be high, at least close to unity; this seems to be the case (Baker 2000). ^{13}CO 2→1 observations will be crucial to further investigate the gas properties in the central 1.5 kpc of NGC 7479 and make comparisons to luminous mergers, where Casoli et al. (1992) and Taniguchi et al. (1999), based on data by Aalto et al. 1995 and Casoli et al., have argued that ^{13}CO 2→1 is also relatively faint and thus ^{13}CO may be depressed, at least in some cases.

We note, however, ^{13}CO 1→0 is not as faint at the ^{12}CO maximum as under the extreme conditions of mergers: Fig. 5 shows the line to be as strong as HCN – it just peaks in a different position. The central $^{12}\text{CO}/\text{HCN}$ line ratio of ~ 20 is on the high side if compared to the range found in the central region of a number of galaxies, where 10 is more typical; however the scatter is very large even among barred starburst spirals (Contini et al. 1997). Still, a value of 20 may be an indication that the amount of warm dense gas in the nuclear region of NGC 7479 is only moderate and confined to a small region.

Diffuse gas is likely to be also important even in the central condensation of NGC 7479. This is indicated by the high values $\mathcal{R}_{12/13}$ reaches away from the curved ‘ ^{13}CO -ridge’ in the central condensation. In these areas, the ^{13}CO lines are much narrower than the ^{12}CO transitions ($150 \text{ km s}^{-1} - 300 \text{ km s}^{-1}$ for ^{12}CO versus $50 \text{ km s}^{-1} - 80 \text{ km s}^{-1}$ for ^{13}CO). These differences in line shape are also obvious from the global single dish spectra (Fig. 8).

Diffuse molecular gas has been detected in the centers of a large number of barred and starburst galaxies such as IC 342 (Downes et al. 1992) or NGC 1808 (Aalto et al. 1994) and, of course, in the bar region of the Milky Way (Dahmen et al. 1998). It has also been detected in the center of the elliptical galaxy NGC 759 (Wiklind et al. 1997) where a low line ratio of 0.4 is indicative of a two component medium made up of dense, cold clumps embedded in a warm, diffuse molecular medium. A scenario where ^{12}CO and ^{13}CO emission arises from separate components was suggested for IC 342 as early as 1990 by Wall & Jaffe. The idea that diffuse gas characterized by ^{12}CO emission of moderate optical depth is important even in regions of extreme star formation, usually associated with large amounts of dense molecular gas, has recently gained credibility even for ultraluminous infrared galaxies (Aalto et al. 1995, Downes & Solomon 1998).

It is interesting to note that the ^{13}CO ridge in the central condensation is precisely aligned with the steepest velocity gradient (derived from ^{12}CO , Fig. 10).

4.3. Production of an ICM by tidal disruption and cloud collisions

Cloud disruption due to the tidal field along a bar is one mechanism that could produce a diffuse ICM, especially close to the central condensation. Another possible source of the ICM are off-center cloud collisions.

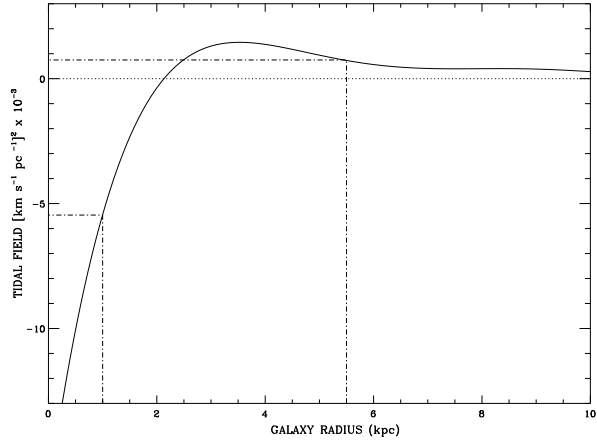


Fig. 11. Tidal field per unit mass and across unit length (see text for explanation) along the bar. The dotted lines indicate the tidal field at radii 1 kpc and 5.5 kpc, which are the semiminor and semimajor axes of the bar. This illustrates the change in tidal force that a cloud on an elongated bar orbit can experience.

(i) *Cloud evaporation due to the tidal field*: As a bound cloud moves in a bar potential or elliptical orbit, the tidal field across it will vary in time. This produces both internal heating of the cloud and clump evaporation from the outer regions of the cloud (Das & Jog 1995). The evaporated cloud mass will become part of the low density, molecular ICM, raising $\mathcal{R}_{12/13}$.

To get a lower estimate of how the tidal field changes over the bar, we first determined the potential of the galaxy from the deprojected K image data (Combes, private communication). The potential was azimuthally averaged to determine $\Phi(r)$, which was fitted with a polynomial function that was used to derive a rotation curve for the galaxy. The mass to luminosity ratio (M/L) was chosen so as to obtain the best fit of the derived rotation curve to that observed. We then used this azimuthally averaged potential to calculate the tidal field over the galaxy. Though this does not give the exact variation of the tidal field across a cloud in the bar potential, it will give a first approximation as to how the tidal field varies. In Fig 11 we have plotted the tidal field per unit mass, across unit length, $t_f = (\partial F/\partial r) (\text{km s}^{-1} \text{ pc}^{-1})^2$ against radial distance r in kpc.

With a projected bar length of approximately 10.4 kpc and width 1.6 kpc (Fig. 1), an inclination angle of 41° and a position angle 25° for the bar (Sempere et al. 1995), the deprojected bar length is about 11 kpc and its width is about 2 kpc (Arnaboldi et al. 1995). So at the semimajor axis distance of $r=5.5$ kpc, $t_f = 0.8 \cdot 10^{-3} (\text{km s}^{-1} \text{ pc}^{-1})^2$ and at the semiminor axis distance of $r = 1$ kpc, $t_f = -5.5 \cdot 10^{-3} (\text{km s}^{-1} \text{ pc}^{-1})^2$. Thus, the tidal field changes from being disruptive at the bar ends to compressive close to the bar center. This considerable change in tidal field,

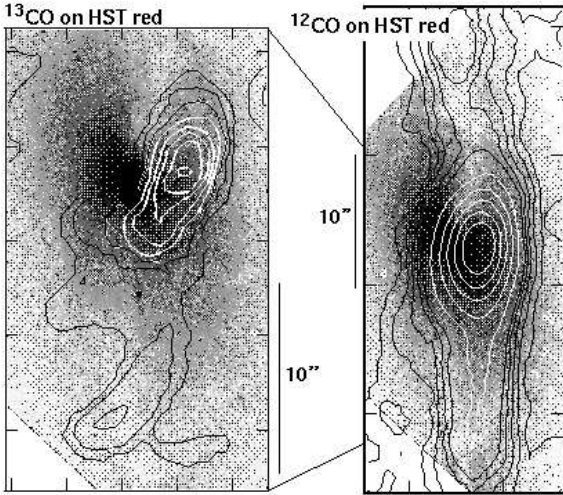


Fig. 12. Superposition of the ^{12}CO distribution (right) and the ^{13}CO distribution on an archival HST (Planetary Camera) red image that shows the shape of the dust lanes.

which is steepest in the central region, may produce significant cloud evaporation, thus leading to large amounts of diffuse gas.

(ii) *Cloud Collisions*: Hydrodynamic simulations have shown that off-center cloud collisions lead to gas being sheared off the colliding clouds, forming trailing extensions in the interstellar medium; the gas then dissipates into the ISM (Hausman 1981). This gas may form part of the diffuse ICM. In bars, the crowding of closed x_1 orbits at the bar ends enhances the cloud collision frequency significantly and also produces shocked gas. Collisions also cause the clouds to lose angular momentum and sink inwards leading to the central buildup of gas. This increased concentration of gas in the centers of starburst galaxies and barred galaxies means the rate of formation of diffuse gas in these galaxies will also be high. NGC 7479 has a strong bar and may have undergone a recent minor merger (Laine & Heller 1999). Thus, the cloud collision rate should be high and there should be a considerable amount of diffuse gas in the central ~ 1.5 kpc.

Distinguishing between the two mechanisms observationally is not easy. The diffuse gas produced by cloud collisions may often be accompanied by shocked, dense gas. Tidally evaporated gas will not have this association. However, diffuse gas is expected to spread over the bar more quickly than dense gas, which will make it difficult to determine its origin. Still, in the future sensitive, high resolution observations of a shock tracer like SiO may be useful to decide this question.

4.4. The Relation between Tracers of Shocks and Star Formation

The S-shaped, complex velocity field of the gas in the bar of NGC 7479 (see Fig. 10) has been convincingly explained by e.g. Laine et al. (1999) as the result of gas streaming motions in a strong bar potential. They further argue that $\text{H}\alpha$, dust lanes, a large velocity gradient and strong ^{12}CO emission more or less coincide. These are all taken to trace, in some sense, shocks, gas compression and star formation.

Including ^{13}CO and the varying line ratios, indicative of at least two different components of molecular gas, (and seeing all the ^{12}CO) leads to a more complex picture. In Fig. 12, we overlay the ^{12}CO (right) and ^{13}CO (left) intensity distributions on an HST red image retrieved from the archive. In the north, where no ^{13}CO is detected outside the central region, ^{12}CO follows the strong dust lane almost perfectly. In the south, the visual dust lane is weaker or more diffuse and the correlation with the ^{12}CO distribution is much less evident. However, the southern ^{13}CO peak coincides with a (faint) peak in a dust lane. South of the center, $\mathcal{R}_{12/13}$ grows when we move upstream (west) across the bar (assuming that the spiral arms are trailing). In other words, the ^{13}CO concentration is located downstream from the ^{12}CO maximum, and possibly also downstream from the peak of the shock, if we identify the ^{12}CO maximum with the shockfront. This may be justified by the close coincidence of the ^{12}CO maximum with the optical dust lane in the north and also by the excellent agreement Laine et al. (1999) find between ^{12}CO peaks (both in the north and in the south) and the maxima in a $J - K$ NIR color map that is an even better indicator of dust than an optical image.

In the central concentration, the course of the dust lanes is not clear. However, here it is the ^{13}CO that very clearly follows the steepest velocity gradient (Fig. 10b), while ^{12}CO is distributed fairly independently of the velocity gradient. ^{12}CO -emitting gas at a velocity between 2280 km s^{-1} and 2340 km s^{-1} traces the velocity gradient somewhat more closely than gas at other velocities (Fig. 10c), but even in this restricted velocity range the ^{12}CO emission does not follow the velocity field as clearly as the ^{13}CO emission does. A number of spectra from the central $15''$ have their emission peak close to 2300 km s^{-1} , and a narrow emission component may be associated with this peak (faintly visible in Fig. 4).

The velocity field based on ^{13}CO is displayed in Fig. 10d). It is even more dramatically S-shaped than the ^{12}CO velocity field. We further note that the ^{12}CO velocity field determined by Laine et al. closely resembles our ^{13}CO velocity field, and that their ^{12}CO distribution in the central $15''$ appears more bent than ours.

This evidence leads us to the following scenario: The ^{13}CO emission and a part of the ^{12}CO emission, especially at mid-velocities, traces dense or at least high column density gas that follows the velocity field and is compressed

in the region with the steepest velocity gradient. We suspect that this region coincides with the central dust lane, which is, however, not clearly visible in the HST image. In terms of ^{12}CO emissivity, this gas component is not dominant enough to clearly reduce $\mathcal{R}_{12/13}$. Also, the dust lane may be fairly narrow and unresolved in our data. Thus, this component is seen most clearly in the ^{13}CO data, but Laine et al. also trace it in ^{12}CO since they are not sensitive to much of the extended emission. The ^{12}CO and ^{13}CO distributions in our maps deviate because the ^{12}CO emission, especially but not exclusively at non-central velocities, is due to diffuse gas that is far less confined to the shock region in the central $10'' - 15''$ ($\sim 2 \text{ kpc}$). The dramatic S-shape in the ^{13}CO velocity field (Fig. 10d) indicates that the strong inner bar of NGC 7479 is the feature dominating the kinematics of the denser gas in this central region. As discussed earlier (Fig. 2), a rotating disk or gas on x_2 -orbits, perpendicular to the main bar axis, is interacting with the bar on the scale of a few hundred pc at the very center.

It is conceivable that the diffuse gas rises to higher altitudes above the plane of the galaxy than the dense gas, which may be less turbulent and more strongly dominated by the bar potential, which is defined by the stellar potential, since most of the dynamical mass is almost certain to be in the form of stars.

Outside the central 2 kpc, the relation between the various tracers changes: both the detached northern and the southern ^{13}CO peaks are found close to, but not coincident with, regions of steep velocity gradients (Fig. 10). The dust lane (and presumably the region of the strongest shock) is now traced well by the ^{12}CO emission. Possibly, the larger overall amount of gas in the central 2 kpc allows a diffuse component to spread throughout this region, while in the outer bar the gas associated with the shock remains diffuse.

It seems possible that the ^{13}CO peaks in the outer bar indicate conditions that are more quiescent and favourable to the formation of bound clouds and ultimately star formation activity. The low value of $\mathcal{R}_{12/13}$ in these complexes suggests that their properties are similar to GMCs in the spiral arms of normal galaxies. The cuts presented by Sempere et al. (1995) indicate that the $\text{H}\alpha$ emission peaks along with the ^{13}CO in the southern condensation, i.e. is offset from the ^{12}CO and main dust lane in this area. If the $\text{H}\alpha$ traces star formation, this shift away from a region that seems to be totally dominated by diffuse gas may reflect that star formation occurs wherever the gas density is high enough, while the proximity to the shock front may play a secondary role. The fact that the ^{13}CO condensations are close to (offset $1'' - 2''$) strong (^{12}CO) velocity gradients need not be a contradiction to quiescent conditions. The peaks of the condensations are downstream of the strongest gradient by several hundred pc. In addition, the interiors of the condensations could be quiescent while the condensations themselves are following a strong

overall large-scale flow. This question, however, requires further study on smaller spatial scales.

Offsets between molecular gas concentrations and dust lanes have recently been reported by Rand et al. (1999) for a part of a spiral arm in M 83. They used ^{12}CO as a tracer, but see only 2% – 5% of the single dish flux in their interferometer map. Thus, they probably filter out the diffuse component, so their ^{12}CO data might trace a dense, clumpy component similar to what we see in ^{13}CO .

5. Conclusions

We have mapped the barred spiral galaxy interferometrically in the $J = 1 \rightarrow 0$ transitions of ^{12}CO , ^{13}CO and HCN. Our main results are as follows:

1. The ^{12}CO map shows a continuous gas distribution all along the bar. Comparison to single dish observation shows that the interferometer does not miss a significant amount of flux. The velocity field derived from the ^{12}CO map is complex, showing the S-shaped isovelocity contours typical of noncircular gas orbits in a strong bar.
2. A high velocity feature is identified close to the center. This may be a ring associated with an Inner Lindblad resonance, a tilted rotating disk fed directly by mass infall along the bar or even an inner bar decoupled from the main bar.
3. ^{13}CO emission is detected in the central condensation, the southern part of the bar and a single location in the northern part of the bar. HCN emission is only detected from the center. The ^{13}CO central emission is offset by $\sim 2''$ from the ^{12}CO and HCN intensity maxima, which are coincident. Along the bar, the most prominent peak of southern ^{13}CO condensation is also clearly offset from the ^{12}CO distribution.
4. The $^{12}\text{CO}/^{13}\text{CO}$ line intensity ratio, $\mathcal{R}_{12/13}$, varies dramatically. Globally ($9 \text{ kpc} \times 2.5 \text{ kpc}$), $\mathcal{R}_{12/13}$ is 20 – 40, a high value compared to typical ratios found in the disk component of galaxies or even central regions of normal galaxies. This indicates a prominent contribution of diffuse, unbound molecular gas with a moderate optical depth in the $^{12}\text{CO}(1 \rightarrow 0)$ transition in both the bar and the center of NGC 7479.
5. On smaller sizescales of $\sim 750 \text{ pc}$, $\mathcal{R}_{12/13}$ exceeds 30 in large parts of the bar, reaching values usually found in starburst mergers. Since values as low as 5 are also found in the bar, close to the ^{13}CO condensation, and since a bar environment is very well mixed, we discard an underabundance of the ^{13}C isotope as a possible explanation of the very high $\mathcal{R}_{12/13}$ found in many places. Instead, this is explained by a dominant component of diffuse gas, readily produced by either tidal disruption or cloud collisions in the bar potential. The large variation in $\mathcal{R}_{12/13}$ is reflected by large changes of likely values of the conversion factor from ^{12}CO intensity to H_2 column density. In the central 1.5 kpc,

the Galactic ‘standard’ conversion factor (SCF) overestimates the gas mass by a factor of up to 10; in ^{12}CO peaks along the bar the discrepancy is even larger. Only in a ^{13}CO complex in the bar we find the SCF to be correct.

6. The offset in the central HCN (and ^{12}CO) peak from the ^{13}CO peak can be attributed to a gradient in kinetic temperature in which the highest gas kinetic temperature is at the position of the HCN peak. This leads to the prediction that the $^{13}\text{CO}(2\rightarrow 1)/(1\rightarrow 0)$ intensity ratio should be higher at the HCN peak than at the ^{13}CO peak.
7. The region along the bar where $\mathcal{R}_{12/13}$ is small might be an area where the conditions are more quiescent, which is also indicated by the narrowness of the lines, both in ^{12}CO and ^{13}CO , found here. If the ^{12}CO ridge along the bar, which coincides closely with the dust lanes, is taken to be the location of the bar shock, the ^{13}CO condensation is behind or downstream this shock, possibly in a region where the disrupted (but also compressed) gas emerging from the shock can form bound molecular complexes. However, the region where the velocity gradient is steepest along the bar does not coincide exactly with either the ^{12}CO or the ^{13}CO distribution. In the center, ^{13}CO traces the steepest velocity gradient much more closely than ^{12}CO . Thus, the relation between the molecular tracers and the shock is complex.

Acknowledgements. The OVRO mm-array is supported in part by NSF grant AST 9314079 and the K.T. and E.L. Norris Foundation.

References

Aalto S., Black J.H., Johansson L.E.B., Booth R.S., 1991, A&A 249, 323

Aalto S., Booth R.S., Black J.H., et al., 1994, A&A 286, 365

Aalto S., Booth R.S., Black J.H., Johansson L.E.B., 1995, A&A 300, 369

Aalto S., Hüttemeister S., Das M., Wall W.F., 1997, in: The central regions of the Galaxy and galaxies, ed. Y. Sofue (IAU Coll. 184), p. 251

Aalto S., Radford S., Scoville N.Z., Sargent A., 1997, in: Galaxy interactions at low and high redshifts (IAU Coll. 186), P. 70

Arnaboldi M., Capaccioli, Capellaro E., et al., 1995, AJ 110, 199

Athanassoula E., 1992, MNRAS 259, 345

Baker A., 2000, PhD Thesis, California Institute of Technology

Binney J., Gerhard O.E., Stark A.A., et al., 1991, MNRAS 252, 210

Bryant P.M., Scoville N.Z., 1999, AJ 117, 2632

Casoli F., Dupraz C., Combes F., 1992, 264, 55

Combes F., Dupraz C., Gerin M., 1990, in: Dynamics and Interactions of Galaxies, ed. R. Wielen (Berlin, Springer), p. 305

Contini T., Wozniak H., Considere S., Davoust E., 1997, A&A 314, L5

Dahmen G., Hüttemeister S., Wilson T.L., Mauersberger R., 1998, A&A 331, 959

Das M., Jog C.J., 1995, ApJ 451, 167

Downes D., Solomon P.M., 1998, ApJ 507, 615

Downes D., Radford S., Guilloteau S., et al., 1992, A&A 262, 424

Friedli D., Benz W., 1993, A&A 268, 65

Friedli D., Benz W., Kennicutt R., 1994, ApJ 430, L105

García-Burillo S., Guélin M., 1995, A&A 299, 657

Groosbol P.J., 1985, A&AS 60, 261

Hausman M.A., 1981, ApJ 245, 72

Hüttemeister S., Aalto S., Wall W.F., 1999, A&A 346, 45

Kenney J.D.P., Wilson C.D., Scoville N.Z., et al., 1992, ApJ 395, L79

Laine S., Heller C.H., 1999, MNRAS 308, 557

Laine S., Shlosman I., Heller C.H., 1998, MNRAS 297, 1052

Laine S., Kenney J.D.P., Yun M.S., Gottesman S.T., 1999, ApJ 511, 709

Langer W.D., Penzias A.A., 1990, ApJ 357, 477

Martin P., Roy J.-R., 1994, ApJ 424, 599

Neff S.G., Hutchings J.B., 1992, AJ 103, 1746

Nilson P., 1973, Uppsala General Catalogue of Galaxies, Acta Universitatis Upsaliensis, Nova Regiae Societatis Upsaliensis, Series V: A Vol. 1

Padoan P., Juvela M., Bally J., Nordlund A., 2000, ApJ 529, 259

Polk K.S., Knapp G.R., Stark A.A., Wilson R.W., 1988, ApJ 332, 432

Quillen A.C., Frogel J.A., Kenney J.D.P., et al., 1995, ApJ 441, 549

Rand R.J., Lord S.D., Higdon J.L., 1999, ApJ 513, 720

Regan M.W., Sheth K., Vogel S.N., 1999, ApJ 526, 97

Reynaud D., Downes D., 1998, A&A 337, 671

Sakamoto K., Okumura S.K., Ishizuki S., Scoville N.Z., 1999, ApJ 525, 691

Scoville N.Z., 1991, In: Combes F., Casoli F. (eds.) Dynamics of galaxies and their molecular cloud distributions. IAU Symp. 146, p. 315

Sempere M.J., García-Burillo S., 1997, A&A 325, 769

Sempere M.J., Combes F., Casoli F., 1995, A&A 299, 371

Strong A.W., Bloemen J.B.G.M., Dame T.M., et al., 1988, A&A 207, 1

Taniguchi Y., Ohyama Y., Sanders D.B., 1999, ApJ 522, 214

Wall W.F., Jaffe D., 1990, ApJ 361, L45

Wall W.F., Jaffe D.T., Bash F.N., Israel F.P., 1991, ApJ 380, 384

Wiklind T., Combes F., Henkel C., Wyrowski F., 1997, A&A 323, 727

Wilson T.L., Matteucci F., 1992, A&ARv 4, 1

Zaritsky D., Kennicutt R.C., Huchra J.P., 1994, ApJ 420, 87